Noncontact atomic force microscopy studies of vacancies and hydroxyls of TiO$_2$(110): Experiments and atomistic simulations

Georg H. Enevoldsen,[1] Adam S. Foster,[2] Mona C. Christensen,[1] Jeppe V. Lauritsen,[1] and Flemming Besenbacher[1]

[1]*Interdisciplinary Nanoscience Center (iNANO) and Department of Physics and Astronomy, University of Aarhus, DK 8000 Aarhus C, Denmark*

[2]*Laboratory of Physics, Helsinki University of Technology, I-02015 Espoo, Finland*

From an interplay of noncontact atomic force microscopy experiments and simulations, we present here a detailed account of atomic-scale contrast encountered in force microscopy of the prototypical metal-oxide surface TiO$_2$(110). We have previously shown for this surface how the atomic-scale atomic force microscopy (AFM) contrast depends crucially on the tip-termination polarity. Here, we extend this finding by also taking into account the influence of the tip-surface imaging distance as controlled by the scanning parameters. Atomic-resolution imaging is shown to be possible in three distinctly different types of contrast modes corresponding to three different types of tip-apex terminations. In the two predominant modes, the AFM contrast is found to be dominated principally by the polarity of the electrostatic interactions between the tip-apex atoms and the O and Ti surface sublattices. A negatively (presumably O$^{\delta-}$) terminated tip generates AFM images in which the positive sublattice (Ti) and bridging hydroxyl (OH) adsorbates are imaged as bright protrusions, whereas a positively terminated tip (Ti$^{\delta+}$) results in AFM images with inverted contrast. Experiments show that the qualitative details of the imaging contrast of the surface signatures are retained at all realistic tip-surface imaging distances for both tips, but a detailed comparison of AFM images recorded at different scanning parameters with calculated site-specific force-distance curves illustrates how the quantitative appearance may change as the surface is probed at closer distances. The third observed imaging mode, which, however, is obtained quite seldom, reflects a tip having a predominantly covalent interaction with the surface atoms, since the resulting imaging contrast is very close to the real topographic structure of the surface. We expect that also for other surfaces with an ionic or semi-ionic character that the atomic-scale AFM contrast depends strongly on the exact nature of the tip apex in a similar way, and the present analysis outlines how all imaging modes can be included in an atomic-scale analysis to reveal the chemical identity of defects and adsorbates on such surfaces.

I. INTRODUCTION

Atomic force microscopy (AFM) is a scanning probe microscopy technique[1] capable of revealing the atomic structure of surfaces and molecules adsorbed on surfaces in real space, even under different environmental conditions.[2–4] As a surface analytical tool, the main importance of AFM derives from the fact that it can be applied to any surface, conducting as well as nonconducting, as opposed to the scanning tunneling microscopy[5] (STM) for which the surface has to be conducting. Especially, when operated in the noncontact mode (nc-AFM or dynamic AFM) under ultrahigh vacuum (UHV) conditions,[2,3] it has successfully been demonstrated that AFM is capable of producing genuine atomic-resolution images of single crystal surfaces.[6] During the last decade, atomic resolution of surfaces and single-atom defects has been reported on a number of insulating surfaces,[4,7] but in many cases, the contrast mechanisms responsible for the nc-AFM images are not fully understood.[8] Recent nc-AFM studies combined with simulations based on density functional theory[9–11] have demonstrated that the contrast in atomically resolved AFM images of compound surfaces should, in general, be considered as a rather complicated convolution between geometrical features pertaining to the surface and a "chemical" contribution. The atomic-scale AFM contrast is determined by the short-range forces which

set in when the AFM tip apex is brought in close proximity of the surface. The short-range forces may thus be dominated by covalent or ionic contributions,[12–15] and the specific nature of this chemical interaction thus depends intimately on the surface and the structure and composition of the tip apex. It is generally accepted that typically only a few atoms participate in the direct bonding to the surface, and experimental experience has shown that most such "nanotips" are fragile and may change frequently due to materials exchange between the surface and tip. Due to the very local nature of the interaction, even small changes can have a dramatic effect on the imaging contrast, as we have previously shown for the TiO$_2$(110) surface.[11] In that paper, it was demonstrated how changes in the atomic arrangement of the tip apex resulted in two predominant types of atom-resolved AFM images of the TiO$_2$ surface, neither of which revealed the true geometrical topography of the surface or its defect and adsorbates. It was also demonstrated how the complementary information obtained from both types of AFM images could be combined to construct a realistic model of the tip-surface interaction and, as a next step, how the information in the AFM images can be used to discriminate between and subsequently chemically identify the prevalent surface defects and adsorbates as oxygen vacancies and hydroxyls on the TiO$_2$(110) surface. As an extension of these studies, we present here a thorough and comprehensive nc-AFM study of the TiO$_2$(110) surface.

From a large data set consisting of more than 500 atom-resolved images taken with a range of different tips, we have managed to group all our atom-resolved images into three categories (contrast modes) determined by the nature of the tip apex. First, we focus on two distinctly different contrast modes for nc-AFM imaging of the $TiO_2(110)$ surface, corresponding to the two predominant types of tip-termination polarities, namely, positive and negative, which enable us to assign the chemical identity to all surface features imaged by nc-AFM on the $TiO_2(110)$ surface. We also discuss a third, but far less frequent, nc-AFM imaging mode which, in contrast to the two predominant imaging modes, yields an image contrast resembling closely the real topography of the hydroxylated $TiO_2(110)$ surface. For each of the predominant contrast modes, we explore the parameters which control the contrast of nc-AFM images, such as the tip-surface imaging distance (amplitude setting, frequency shift set point). The experimental observations are then compared to theoretical calculated spectroscopic curves, and using this approach, we can explain the contrast mechanisms for this surface. The present study may thus serve as a general reference for AFM studies of the $TiO_2(110)$ surface, which has evolved into the most studied metal-oxide surface in recent years.[16,17] The present study also provides a detailed account of the dependencies of both the tip polarity and tip-surface imaging distance on the actual nc-AFM contrast on a metal oxide, and the results are expected to be of general applicability for AFM imaging of ionic or semi-ionic compound materials and metal oxides, in particular. So far, a limited number of atom-resolved studies have been reported for ionic materials, e.g., NaCl,[18] and KBr,[19] or metal oxides such as $MgO(001)$,[20,21] $CeO_2(110)$,[22,23] or $Al_2O_3(0001)$,[24] and in most cases, the imaging contrast is associated with only one of the sublattice ions when the surface is probed with nc-AFM in the attractive force regime. Finally, we show that nc-AFM can directly image the dynamic process of the splitting of paired hydroxyls on the $TiO_2(110)$ surface along the $[-110]$ direction and the diffusing of single hydroxyls along the same direction, consistent with the findings of the previous STM study.[25]

II. METHODS

A. Experimental details

The experimental setup consists of an ultrahigh vacuum (UHV) chamber with a base pressure below 1×10^{-10} mbar equipped with an Omicron variable-temperature AFM/STM. The nc-AFM control unit was enhanced by adding a digital NanoSurf EasyPLL controller unit for improved frequency shift detection. The cantilevers used for the experiments were all uncoated silicon cantilevers (Nanosensors, type NCH) with resonance frequencies in the range 240–300 kHz and spring constants of ~19 N/m. We found that it was very useful to use Ar^+ ion bombard ($E \sim 2$ keV, fluence ~3.8 $\times 10^{15}$ cm^{-2}) of the tip both as an initial cleaning procedure of the tip and as a means to "sharpen up" a blunt tip. The experimental setup did not allow for a direct grounding of the tip during ion-bombardment process, but, although this

may have reduced the efficiency of the ion-bombardment process, this did not lead to any permanent charging of the tip.

The images presented in this paper were all taken using noncontact AFM (nc-AFM) operated in the frequency modulation mode (or dynamic AFM),[26] where the tip-cantilever system is excited at its first mechanical resonance frequency to a constant amplitude in close proximity of the surface. The forces arising between the tip and the surface, e.g., van der Waals (vdW), chemical, and electrostatic forces, cause a shift in the resonance frequency of the tip-cantilever system relative to the free resonance frequency (referred to as frequency shift, or simply *df*). For the experiments presented here, we probed the $TiO_2(110)$ surface in the *attractive* regime, which caused the resonance frequency to shift down, resulting in a *negative* frequency shift. All the reported frequency shift values are negative, with larger values meaning more negative values. As the tip was raster scanned across the surface, variations in the frequency shift signal were recorded and used to generate the nc-AFM images, either as the direct imaging signal (constant height images) or, as presented here, as a feedback-loop signal controlling the tip-surface distance to maintain a preset frequency shift set-point signal (constant frequency shift images). In this way, the tip traces the surface on a contour of constant frequency shift, and the changes in tip-surface distance, controlled by the feedback-loop, are used as the imaging signal, generating a "topographic" image of the surface. The bias voltage applied to the surface relative to the tip (U_{bias}) was monitored regularly and adjusted to minimize the electrostatic forces arising from the contact potential difference (CPD).[27,28] We found that the CPD changed significantly, ranging from a value of $2-3$ V for a new tip to $0.5-1$ V for a tip cleaned with the Ar^+ ion-bombardment process described above.

The frequency shift set point at which the optimal atomic resolution could be obtained varied significantly from experiment to experiment. In this paper, we present nc-AFM images taken with a wide range of different tips, recorded at negative frequency shift set points ranging from a few hertz to a few hundred hertz, reflecting the fact that the macroscopic sharpness (tip-apex radius) of the AFM tip and therefore the long-ranged vdW forces varied from tip to tip and from experiment to experiment.[9] Surprisingly, we observed that the macroscopic sharpness of the tip did not affect the quality of the atomic resolution on flat terraces of the surface to any great extent, and, to a certain degree, relatively blunt tips generally provided more stable nc-AFM imaging. Therefore, for constant frequency shift images recorded with different tips, the frequency shift set point cannot generally be used alone as an indication for how closely the tip probes the surface. When comparing experimental nc-AFM images with theoretically calculated images, the variations in the tip sharpness, as evident from the wide range of frequency shift set points, are, however, not a problem, since the long-ranged vdW forces can be accounted for rather precisely in the theoretical modeling (see next section). We found that the variation of the vdW contribution due to the macroscopic tip shape did not change the qualitative appearance of the resulting force curves, and the variations in the contrast described in this study should therefore be valid for both sharp and

blunter tips. An exact quantitative correspondence of the image corrugation may easily be obtained for images obtained with a specific tip by fitting the vdW contribution as was done in, e.g., Ref. 11.

The TiO$_2$(110) crystal was initially cleaned using several cycles of Ar$^+$ ion bombardment ($E \sim 800$ eV, fluence $\sim 1 \times 10^{16}$ cm^{-2}) followed by annealing ($T \sim 950$ K, $t \sim 20$ min). After initial cleaning, it was sufficient with a single cleaning cycle prior to each experiment to produce a clean and impurity-free surface suitable for experiments, all of which were carried out at room temperature.

B. Theoretical calculations

The calculation of the tip-surface interactions on the microscopic scale was performed using static atomistic simulations, as implemented in the two-dimensional periodic codes MARVIN.[29] This simulation technique uses point charges and polarizable shells to represent atoms and pair potentials to represent atomic interactions. The rutile TiO$_2$(110) surface was represented by a ($6 \times 3 \times 3$) unit cell which was thick enough to converge the surface structure and large enough to avoid spurious interactions between adsorbates. We used a metal-oxide cluster tip model, namely, a 64-atom MgO cube. Such a cluster tip model provides a well-defined nanoprobe where the cube can be oriented to expose either a positive (Mg^{2+}) or negative (O^{2-}) electrostatic potential from the tip apex.[30] The top 20 atoms of the tip and the bottom layer of the surface were kept frozen during simulations to represent the bulk, while all other atoms were allowed to fully relax with respect to interatomic forces. The pair potential parameters for the TiO$_2$(110) surface and its interaction with water were taken from Ref. 31, and these have been extensively tested against both first-principles calculations and experimental data. The remaining parameters for the tip and tip-surface interaction were obtained from Ref. 32. We also considered several other plausible tip models in the simulations, including some based on SiO$_2$ and TiO$_2$, including water tip-apex contamination. These other tip models did not change the results presented here significantly, which shows that the MgO tip represents a reliable and general model of an ionic tip due to the dominance of electrostatics in the imaging interactions.

Once the models of the tip and surface are established, we define a three-dimensional grid over the surface and calculate the force between tip and surface at each point on this grid. This calculation provides the microscopic forces between tip and surface, but in order to generate images which can be compared to experiment, it is important to include the long-range macroscopic vdW interaction between the tip and surface. This contribution acts as a background attractive force, which is important in terms of reproducing the experimentally observed frequency changes, but is independent of the identity of the tip-apex atom and the surface atom beneath and does not play a role in atomic displacements. This means that the interactions can be calculated separately and only combined for the final stages of modeling. The vdW force is mainly determined by the radius of the macroscopic part of the tip and the Hamaker constant of the system, and for

simplicity, the macroscopic part of the tip is represented by a cone with a sphere at the end into which the nanotip is embedded.[33] Since the original tip is very likely to consist of oxidized silicon, we fix the Hamaker constant to the value for SiO$_2$-TiO$_2$,[34] and we were then able to fit the tip-apex radius to reproduce the experimentally measured surface contour contrast [defined as the corrugation of the Ti(5c) relative to the O(2c) rows, $\Delta C_{\text{Ti-O}}$] at the set point for the constant frequency change. Microscopic and macroscopic forces are combined to provide a detailed map of the force across the surface. This map is then used as input in a simple model[33] of the cantilever oscillations using experimental parameters to provide the change in frequency (frequency shift) of the cantilever at a given tip-surface imaging distance. These data can subsequently be either directly used to produce an image at constant height or interpolated to produce a topographic image at constant frequency change. Frequency change curves (df vs distance) are extracted directly from calculated images by plotting the frequency change as a function of distance at a specified lateral position in the image.

III. RESULTS AND DISCUSSION

A. Rutile TiO$_2$(110) surface

Figure 1(a) shows a typical large-scale nc-AFM image of the rutile TiO$_2$(110) surface recorded at room temperature some time after preparation. The image reveals a characteristic striped pattern consisting of bright parallel rows separated by ~ 0.65 nm. This pattern reflects the atomic arrangement of the TiO$_2$(110) surface as depicted in the ball models in Figs. 1(b) top view) and 1(c) (side view), where alternating rows of twofold coordinated bridging oxygen atoms [O(2c)] and fivefold coordinated in-plane titanium atoms [Ti(5c)] located along the [001] direction form a (1×1) surface structure with a periodicity of 0.649 nm along the [-110] direction. Also visible in Fig. 1(a) are several bright protrusions located in between the bright rows. From the extensive literature available on the TiO$_2$(110) surface,[11,35,36] it is well known that this surface, when prepared under standard UHV conditions, is not perfectly stoichiometric. Oxygen atoms are removed from the TiO$_2$(110) surface during the cleaning cycles, reducing it slightly, and as a result, unoccupied O(2c) sites arise, referred to as bridging oxygen vacancies (O-vac).[35] These oxygen vacancies are known to be very reactive, and they react readily with molecular water,[37] which is ever present in the residual gas even under extreme UHV pressures, adsorbed on the surface. The reaction causes the water molecules to dissociate in the vacancies followed by proton transfer to the neighboring O(2c), resulting in the formation of paired side-by-side hydroxyl groups, referred to as double hydroxyls (dOH).[25,36] From the literature, it is also well known that these dOH are not stable over time, but through an interaction with additional water molecules from the residual gas phase, they split up and form isolated single hydroxyl groups (sOH).[25,38] In a recent letter, we showed how O-vac defects and adsorbates such as sOH and dOH can be distinguished in nc-AFM experiments,[11] and
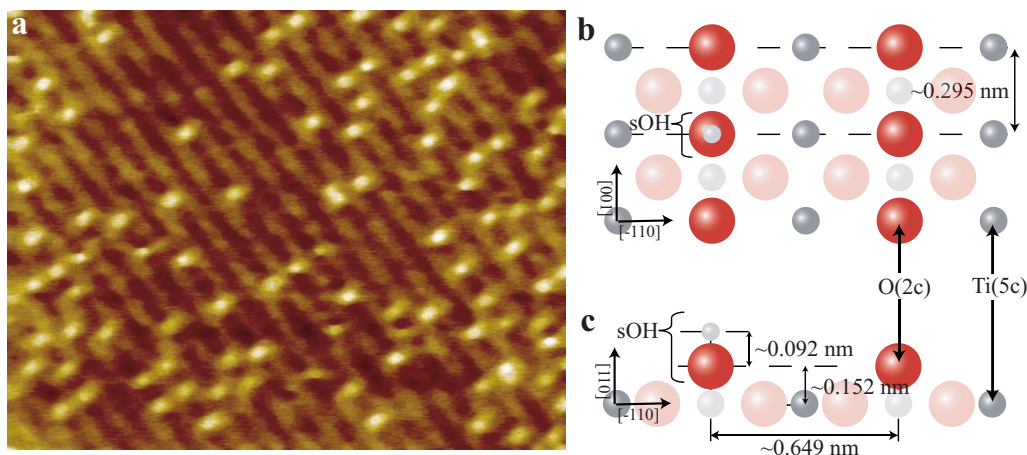
FIG. 1. (Color online) (a) nc-AFM image (15×20 nm^2) of the TiO$_2$(110) surface. Ball models of the TiO$_2$(110) surface are depicted in (b) top down and (c) side view, respectively. Dark red balls (large, black): Twofold coordinated bridging oxygen atoms [O($2c$), formally O^{2-}]. Light red balls (large, light gray): In-plane threefold coordinated oxygen atoms. Dark silver balls (small, dark gray): In-plane fivefold coordinated titanium atoms [Ti($5c$), formally Ti^{4+}]. Light silver balls (small, light gray): Sixfold coordinated titanium atoms. White balls (small, white): Hydrogen atoms. Distances are based on Refs. 35, 55, and 56.

we find that even under extremely good UHV conditions with a measured partial pressure of H$_2$O in the low 10^{-12} mbar range, the transformation from a freshly prepared TiO$_2$(110) surface primarily covered with O-vac to a fully sOH hydroxylated surface occurs within the first 2 h after preparation. Additionally, we find that the initial coverage of O-vac increases slightly with the number of cleaning cycles, in accordance with Ref. 36, and for the experiments presented here, it was estimated to be around 5% per surface unit cell. The results presented in the following therefore reflect nc-AFM images of the TiO$_2$(110) surface in the hydroxylated state, where the predominant surface defects are sOH.

B. Image mode switching

When imaging the TiO$_2$(110) surface, primarily two types of nc-AFM imaging contrast modes were obtained as shown in Figs. 2(a) and 3(a). In both cases, the characteristic bright-dark striped pattern associated with the (1×1) surface structure is clearly resolved. However, upon close inspection, the two images are seen to differ significantly, despite the fact that they both represent the exact same surface. In both images, the surface shows a small population of defects. In Fig. 2(a), additional bright protrusions appear in between the bright parallel rows, similar to Fig. 1(a), whereas Fig. 3(a) shows additional dark holes located in registry with the bright rows. We identify the defects as sOH and dOH groups as indicated in the images, in accordance with the results we presented in a previous work.[11] From the expected position of the sOH and dOH groups (see Fig. 1), it is therefore clear that the ionic sublattice imaged bright differs in the two images. We thus conclude that the Ti($5c$) rows are imaged bright in Fig. 2(a), despite their lower geometric positions, with the OH groups imaged as bright protrusion in between the bright Ti($5c$) rows. Note that this image contrast closely resembles the somewhat counterintuitive way the TiO$_2$(110)

surface is imaged by STM due to electronic effects.[36] Oppositely in Fig. 3(a), the O($2c$) rows are imaged bright with both sOH and dOH groups imaged as dark holes in registry with the O($2c$) rows.

The fact that the TiO$_2$(110) surface can be imaged in two such complementary contrast modes as shown in Figs. 2(a) and 3(a) can be traced back to the electrostatic polarity of the imaging tip apex. A negatively terminated tip, i.e., an anion (e.g., O$^{\partial-}$), generates an image where the Ti($5c$) rows are imaged bright and the O($2c$) rows imaged dark, whereas a positively terminated tip, i.e., a cation (e.g., Ti$^{\partial+}$) generates an image with dark Ti($5c$) and bright O($2c$) rows. The physical reason for these two complementary contrast modes can be explained from the simple picture of additional electrostatic forces arising between the charged tip-apex atom and the surface ions. A positively charged tip gives rise to an additional attractive interaction with the negatively charged oxygen anions in the surface, causing a larger negative frequency shift, and the O($2c$) rows will thus appear bright. The sOH and dOH are polarized entities exposing the positive hydrogen proton of the hydroxyl to the AFM tip, and the O-vac are "less negative" than the O($2c$) rows, which gives them the same type of contrast as the positive Ti($5c$) atoms, in this case, dark relative to the bright O($2c$) rows. Conversely, if the polarity of the tip-apex atom is switched from positive to negative, so is the resulting contrast of all species, explaining the characteristic inverse relationship of the two contrast modes shown in the images in Figs. 2(a) and 3(a).

From our experimental results, we find that it is possible to induce the change between the contrast modes by gently touching the surface with the tip, thereby rearranging and/or changing the tip-apex atoms so that the polarity of the outermost tip atom is switched from positive to a negative ion or vice versa. Figure 4 is unique since it depicts an atomically resolved nc-AFM image of the hydroxylated TiO$_2$(110) surface recorded at a close tip-surface distance, which induced a sudden tip change, resulting in both of the above described
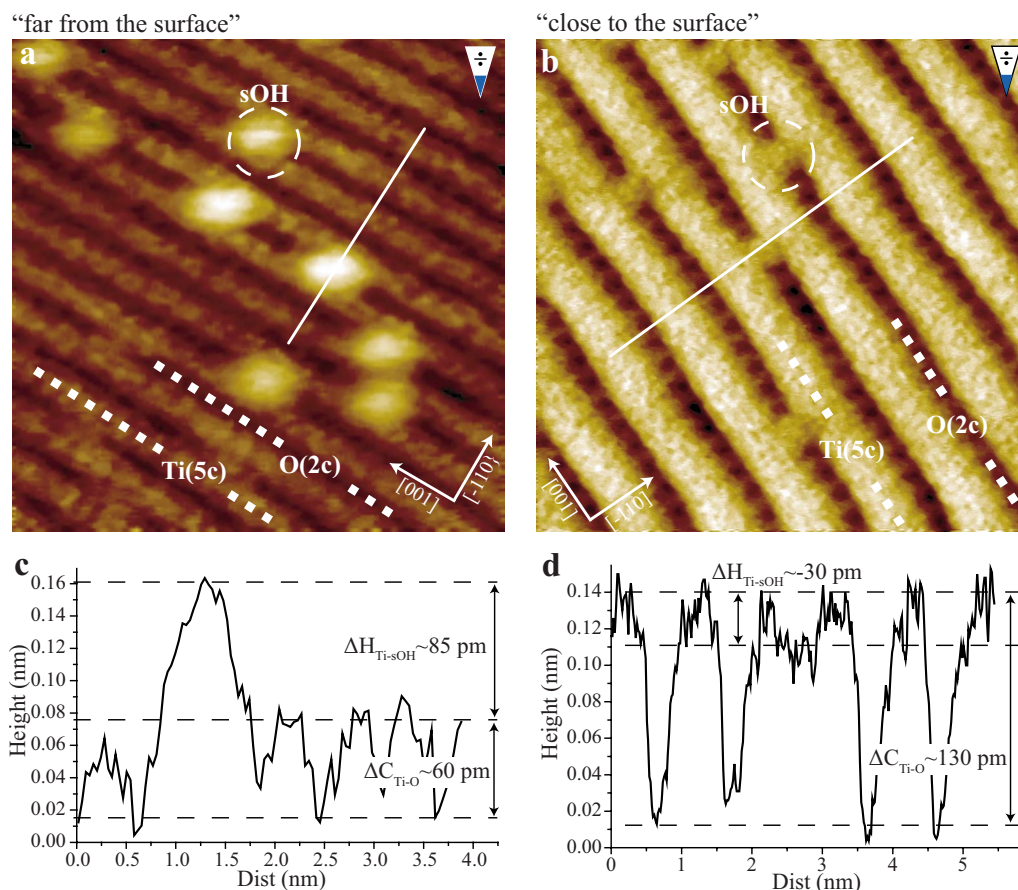
FIG. 2. (Color online) [(a) and (b)] Constant frequency shift nc-AFM images of the $TiO_2(110)$ surface [(a) is a cutout of Fig. 2(a) of Ref. 11]. In both images, the Ti(5c) rows are imaged as bright parallel lines with sOH imaged as bright protrusions located in-between. [(c) and (d)] Cross-section graphs taken along the white solid lines in the [−110] direction in (a) and (b), respectively. Imaging parameters (IPs) for (a) (for (b)) are $df = -45$ Hz (-95 Hz), $Ampl_{p-p} \approx 25$ nm (25 nm), $U_{bias} = 0.93$ V (0.76 V), and size $= 7 \times 7$ nm^2 (7×7 nm^2).

imaging modes being resolved within the same image. The image contrast of the bottom part of the image in Fig. 4 is the same as that of the image in Fig. 3(a), where dark holes associated with sOH groups are imaged scattered along and in registry with the bright O(2c) rows, whereas the image contrast of the upper part is the same as that of the image in Fig. 2(a), with bright protrusions also associated with sOH groups are imaged lying in between the bright Ti(5c) rows. At the point indicated by the lower horizontal white dashed line, the tip probably came in close contact with the surface, causing the atoms forming the tip apex to rearrange, resulting in a semiunstable tip. This event produced a fussy contrast for a short period (a few line scans), but relatively quickly the tip-apex stabilized, and good imaging contrast was recovered. The graph in the left in Fig. 4 shows a cross-sectional scan of the nc-AFM image, parallel to the slow scan direction indicated by the vertical white solid line. It is clear that the change in imaging contrast is associated with a "tip-jump," where the feedback loop instantly retracts the tip, caused by an alteration of the outermost tip atoms. The change in height is, however, relatively small, only ~110 pm, indicating that the change in the tip-apex conformation takes place on the single-atom level, and most likely, a single oxygen anion has been picked up from the surface

and added to the tip apex, causing the tip jump and switching the polarity of the tip-apex atom from positive to negative. After the tip change, the imaging atom on the tip apex is no longer the same, and hence the imaging site on the tip is no longer the same. This change is also evident in the image in Fig. 4, as the bright O(2c) rows in the lower part of the image do not align with the dark O(2c) rows in the upper part.

In the following, the imaging contrast modes in the lower and upper parts of the image in Fig. 4 will be referred to as hole mode and protrusion mode, respectively, referring to the contrast with which the sOH are imaged. For both the protrusion mode and hole mode, we observed variations in contrast corrugation. We find that the corrugation between the Ti(5c) and O(2c) rows (ΔC_{Ti-O}), and also the relative height or depth of O-vac, sOH, and dOH, may vary significantly depending on the nc-AFM scanning parameters and on the state of the tip. These dependencies may significantly complicate the interpretation of the AFM images and lead to confusion about the state of the surface and the prevalent types of defects or adsorbates,[39] and in the following, we will therefore provide a detailed and thorough analysis of both scenarios.
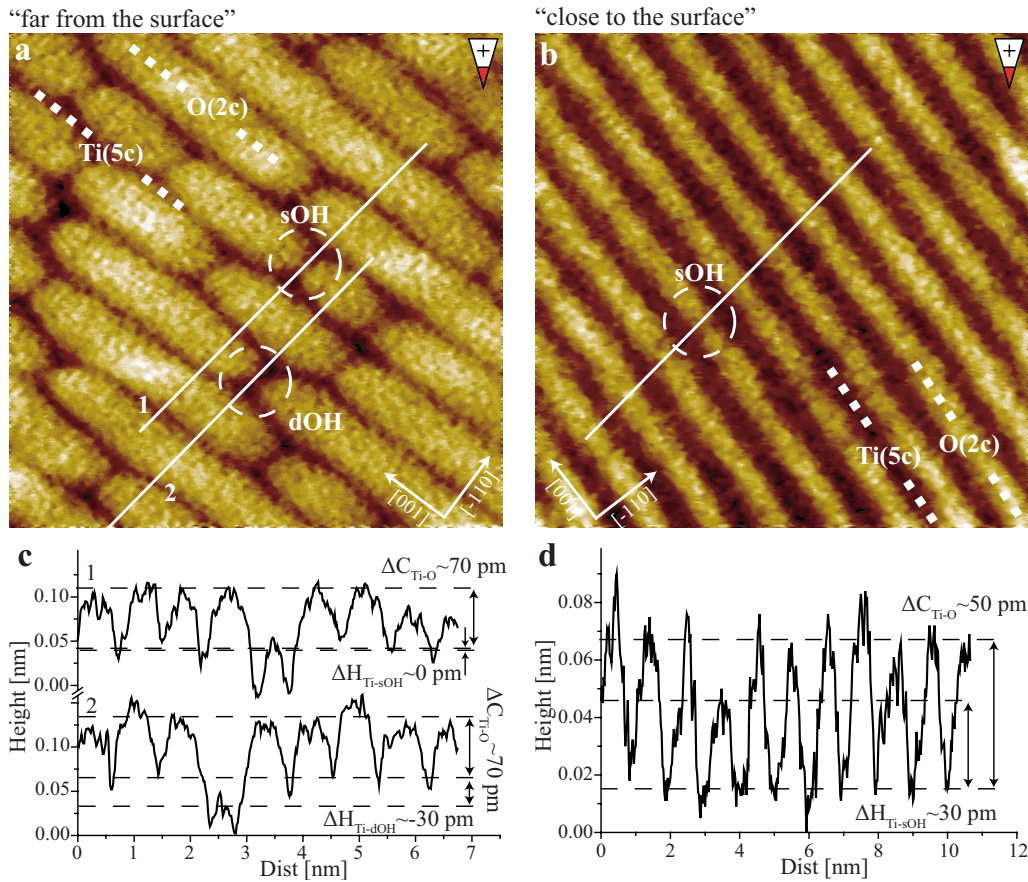
FIG. 3. (Color online) [(a) and (b)] Constant frequency shift nc-AFM images of the $TiO_2(110)$ surface. In both images, the O(2c) rows are imaged as bright parallel rows, with sOH and dOH [(a) only] imaged as dark holes in registry with these bright rows. [(c) and (d)] Cross-section graphs taken along the white solid lines in the [−110] direction in (a) and (b), respectively. IPs for (a) (for (b)) are $df=$ −34 Hz (−27 Hz), $Ampl_{p-p} \approx 20$ nm (20 nm), $U_{bias}=0.95$ V (2.18 V), and size=7×7 nm² (10×10 nm²).

C. Negatively terminated tip (protrusion mode)

Figures 2(a) and 2(b) show two atom-resolved AFM images recorded with a negatively terminated tip in the protrusion mode at a large and small tip-surface imaging distances, respectively. In both images, we identify the bright rows as the Ti(5c) rows, the dark rows in between as the O(2c) rows, and the bright protrusions lying in between the bright rows as sOH. The two images are, however, markedly different on a more quantitative level. Both ΔC_{Ti-O} and the height of the sOH relative to the Ti(5c) rows (ΔH_{Ti-sOH}) differ in the two images. The solid white lines in Figs. 2(a) and 2(b) are represented as cross sections in Figs. 2(c) and 2(d), respectively, and from these graphs, ΔC_{Ti-O} is measured to be ~60 pm at a large tip distance and increasing to ~130 pm at a close tip distance. The corresponding values for ΔH_{Ti-sOH} are measured to be ~85 and ~−30 pm, respectively. This finding implies that even though the polarity of the imaging tip-apex atom is identical in the two images, there is a significant difference of nearly a factor of 2 in ΔC_{Ti-O}, and ΔH_{Ti-sOH} even changes sign.

To analyze further how the image contrast varies as a function of tip-surface imaging distance, we have calculated spectroscopic df vs distance curves. The graph in Fig. 5(a) shows a set of five df vs distance curves for the negatively
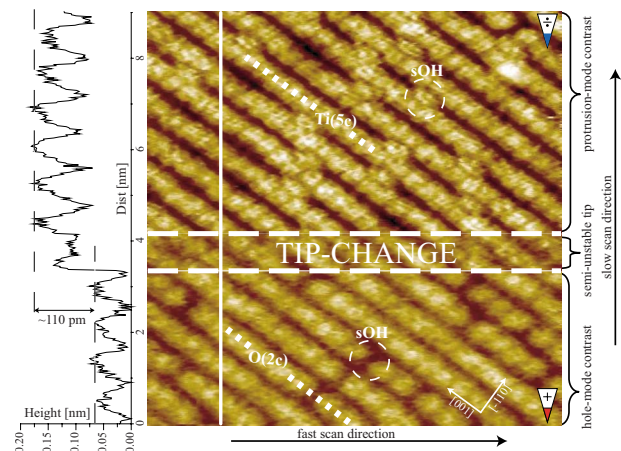

FIG. 4. (Color online) Atomically resolved constant frequency shift nc-AFM image of the $TiO_2(110)$ surface, recorded ~4 h and 12 min after preparation. White dashed circles and dotted lines indicate the position of sOH, O(2c), and Ti(5c) rows, as indicated. The image has been corrected by a line-by-line first order polynomial fit along the fast scan direction for better color contrast. To the left is a cross section taken along the solid white vertical line of the raw-data image. IP: $df=−306$ Hz, $Ampl_{p-p} \approx 20$ nm, $U_{bias}=$ −0.23 V, and size=9×9 nm².
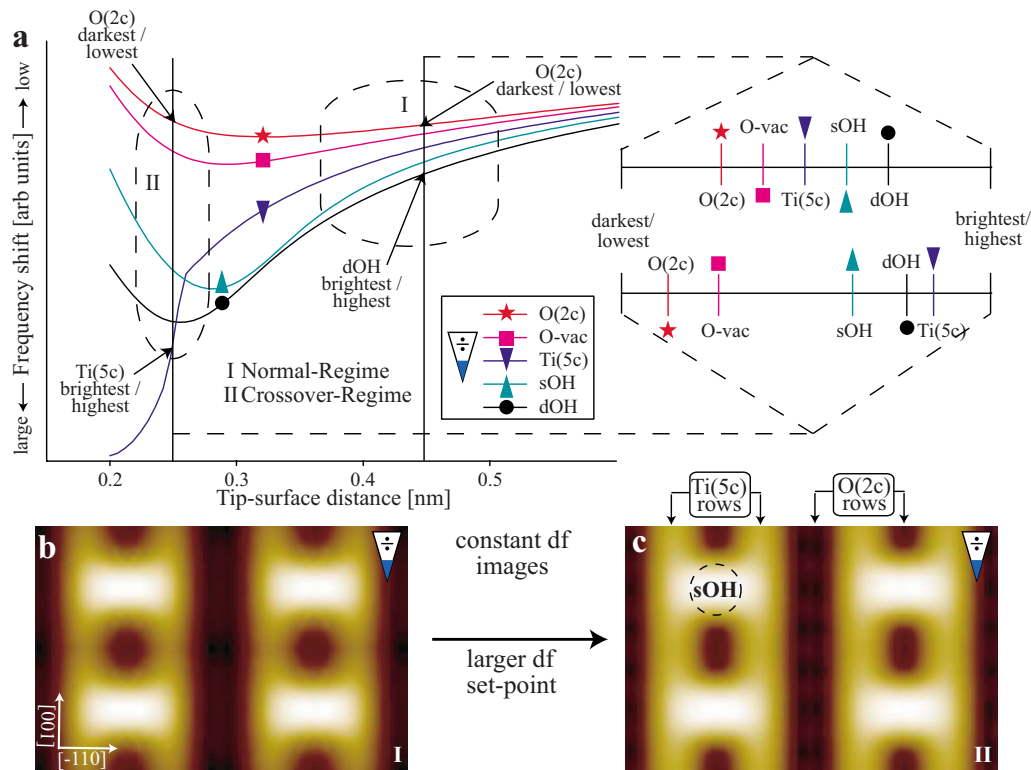
FIG. 5. (Color online) (a) Graph with five df vs distance curves used for identifying the imaging contrast of the different species on the surface as a function of tip-surface separation distance. The zero-point for the x axis is the relaxed position of the O(2c) atoms. The vertical guidelines at $x \sim 0.25$ nm and $x \sim 0.45$ nm have been rotated and are depicted on the right showing the relative cross points for the different curves. [(b) and (c)] Simulated constant frequency shift images of four sOH equidistantly placed along every second O(2c) rows. (c) was simulated at a larger (more negative) frequency shift set point than (b). Image size=2.6×1.8 nm^2

terminated tip calculated over the prevalent sites on the surface. For completeness, we consider both the O(2c) and Ti(5c) sublattices as well as O-vac sOH and dOH[40] sites. The force curves were calculated using a "standard" vdW contribution from the macroscopic tip shape as discussed in Sec. II. The relative positions of the force curves were not affected by changes in the vdW contribution, and the qualitative behavior described by the df vs distance curves is therefore generally valid for any type of macroscopic tip shape. The key to understand the df vs distance graph in Fig. 5(a) is to interpret it in a constant height picture. It should be noted that the experiments presented here were not carried out in the constant height mode, but the contrast in constant height images and constant frequency shift images, as recorded here, are qualitatively similar when imaging flat surfaces.[7] We can thus analyze the df vs distance graphs within a constant height model, in which tips with different vdW contributions (sharpness) are easier to compare, and directly compare such df vs distance graphs qualitatively with the results from our experimental nc-AFM images. The image contrast, for a given tip-surface imaging distance, can be estimated by comparing the relative cross points between a vertical guideline [as shown twice in Fig. 5(a)] and the site-specific df curves. The inserted vertical guidelines at ~ 0.45 and ~ 0.25 nm reflect the two images in Figs. 2(a) and 2(b), corresponding to a large and small tip-surface imaging distances, respectively. For clarity, the sections have been

rotated and depicted in the right to better illustrate the relative positions of the crossing points of the five site-specific df curves. At the large tip-surface imaging distance of ~ 0.45 nm, the different chemical features on the TiO$_2$(110) surface would be imaged: dOH, sOH, Ti(5c), O-vac, O(2c), in order of decreasing brightness or equivalently decreasing height. This brightness or height ordering of the different species agrees perfectly with the detailed analysis in our previous study,[11] as well as with the image and corresponding cross sections depicted in Figs. 2(a) and 2(c), respectively. We will therefore subsequently refer to the tip-surface imaging distance range where this ordering occurs as the "normal regime." To verify the direct comparison between the constant height analysis of the df vs distance graph and our experimental constant frequency shift images, we simulated a constant frequency shift image (see Sec. II) in the normal regime, which is shown in Fig. 5(b). The contrast of the simulated image matches the analysis presented above, with the sOH being significantly brighter than the Ti(5c) row, which is imaged bright relative to the dark O(2c) rows.

At a shorter tip-surface imaging distance of ~ 0.25 nm, the order of df curves crossing the vertical guideline changes. Now, the Ti(5c) rows are imaged with the brightest intensity (e.g., highest), followed by dOH, sOH, O-vac, and O(2c) in order of decreasing height, with the sOH and dOH being imaged only slightly lower than the Ti(5c) rows. Also, the ΔC_{Ti-O} would be much larger as compared with the situ-

ation for the larger tip-surface imaging distance. This brightness or height ordering is in excellent agreement with the experimental small tip-surface distance image and cross-section graph shown in Figs. 2(b) and 2(d), respectively. In the following, we refer to the tip-surface imaging distance range, where the contrasts for sOH (and dOH) and Ti(5c) are comparable, as the "crossover regime." In Fig. 5(c), a simulated constant frequency shift image in the crossover regime is depicted, and the qualitative agreement with the experimental nc-AFM results is evident. The contrasts for the sOH and the Ti(5c) are now comparable, with the sOH being only slightly brighter than the Ti(5c), and the contrast difference between the Ti(5c) and the O(2c) rows is significantly larger, as compared with the simulated normal regime image in Fig. 5(b). Also, if we compare the two simulated images in Figs. 5(b) and 5(c), it is evident that the apparent width of the Ti(5c) rows is larger for the crossover-regime image. This difference is not directly visible from the df vs distance curves in Fig. 5(a), but it matches perfectly with the results from the experimental images in Figs. 2(a) and 2(b).

The two images in Figs. 2(a) and 2(b) and the df vs distance graph in Fig. 5(a) indicate that (for the protrusion mode) the $\Delta C_{\text{Ti-O}}$ and the $\Delta H_{\text{Ti-sOH}}$ are coupled, in the sense that a larger $\Delta C_{\text{Ti-O}}$ is coupled to a smaller or more negative $\Delta H_{\text{Ti-sOH}}$. This point will be analyzed in more detail below. It is somewhat unexpected that the Ti(5c) rows can be imaged higher than the sOH and dOH groups even though the Ti(5c) atoms geometrically reside approximately 0.23 nm lower [see Fig. 1(d)]. This point, however, simply underlines the fact that both the tip-surface imaging distance, the chemical identity of the surface atoms, tip, and surface relaxation and, particularly for compound oxide surfaces such as TiO$_2$, the electrostatic polarity of the surface atoms are all important parameters in determining the resulting nc-AFM imaging contrast.[41]

It should be noted that for the simulated images, we could not probe the full tip-surface distance range of the crossover region in Fig. 5(a) and reach the point where the Ti(5c) rows are imaged as the brightest in images. This difficulty is due to the onset of a sharp jump in the force curve over the Ti(5c) site, which prevents a stable numerical solution of the cantilever dynamics. This jump is very dependent on the exact structural configuration and chemistry of the tip apex,[42] which are unknown in the experiments, and may be considered a technical limitation of the simulations. It should also be noted that the relatively high density of defects in the constant frequency shift simulated images makes an absolute comparison of contrast between defects and ideal surface sites, e.g., $\Delta H_{\text{Ti-sOH}}$, somewhat difficult, as there is a risk of a significant degree of cross-talk. The simulated images presented here are only meant as supporting material for the df vs distance graph, which holds the real physical information. Absolute contrast or height should be measured with respect to surface sites far from the OH group.[11]

D. Positively terminated tip (hole mode)

Figures 3(a) and 3(b) depict two images of the TiO$_2$(110) surface recorded with a positively terminated tip in the hole-mode contrast at a large and small tip-surface imaging distances, respectively. It is noted that the frequency shift set point at which the two images were recorded is almost equal, perhaps even suggesting that Fig. 3(b) was recorded closer to the surface than Fig. 3(a). The images were, however, recorded with different tips, and a direct comparison of the frequency shift set points is therefore ambiguous, whereas the analysis presented in the following justifies the above classification. In both cases, the contrast is now inverted compared to Figs. 2(a) and 2(b) and we now identify the bright and dark rows as the O(2c) and the Ti(5c) rows, respectively, and the species visible as dark holes in registry with the bright O(2c) rows are identified as sOH and dOH (as illustrated in the images). Again there is a significant difference in the relative levels of contrast associated with the sublattices and surface species depending on the minimum tip-surface imaging distance. In Fig. 3(a), the sOH and dOH are imaged as well-defined dark holes in registry with the bright O(2c) rows. The cross sections shown in Fig. 3(c), indicated by the two white solid lines, reveal that the depth associated with the dOH is noticeably larger as compared with the depth of sOH. The $\Delta C_{\text{Ti-O}}$ is measured to be $\sim$70 pm, and the height of the sOH and dOH defects measured relative to the dark Ti(5c) rows is found to be $\sim$0 and $\sim$−30 pm, respectively. The image in Fig. 3(b) is striking in the sense that the surface now may seem defect- and adsorbate-free, i.e., reflecting a perfectly stoichiometric TiO$_2$(110) surface, but this is not the case. The surface is in the same chemical state as the images in Fig. 3(a), and a careful analysis of the corresponding cross-section graph, shown in Fig. 3(d), indeed reveals a shallow pit located in one of the bright O(2c) rows representative of a sOH. The $\Delta C_{\text{Ti-O}}$ and $\Delta H_{\text{Ti-sOH}}$ are measured to be $\sim$50 and $\sim$30 pm, respectively. The image in Fig. 3(b) shows that the sOH can appear with roughly the same height as the O(2c) rows at small tip-surface imaging distances, which effectively makes them invisible, and one might erroneously be left with the impression that the surface is defect-free. We have often recorded images at fairly long time after the initial surface preparation, which often only depict bright parallel rows with no additional species present on the surface, which again might indicate a perfectly stoichiometric surface. The only way of achieving such a surface state from the initially prepared surface is by hydroxylating all O-vac, and then stimulating the desorption of the hydrogen adatoms from the remaining hydroxyl groups, e.g., by applying a large bias voltage ($\sim$3 V) as demonstrated in previous STM experiments.[13,43] We always use moderate bias voltages in the range $\pm$1 V, so this effect cannot account for our apparent stoichiometric surfaces.

The graph in Fig. 6(a) presents the calculated df vs distance curves for O(2c), Ti(5c), O-vac, sOH, and dOH[40] sites for a positively terminated tip. Again, the vertical guideline at $\sim$0.45 nm represents the large tip-surface imaging distance, and it is seen that the O(2c) rows are imaged as the highest followed by the O(vac), Ti(5c), sOH, and dOH in order of decreasing height, with the Ti(5c) and the sOH being imaged at almost the same height. This finding is in perfect agreement with the experimental observations in Fig.
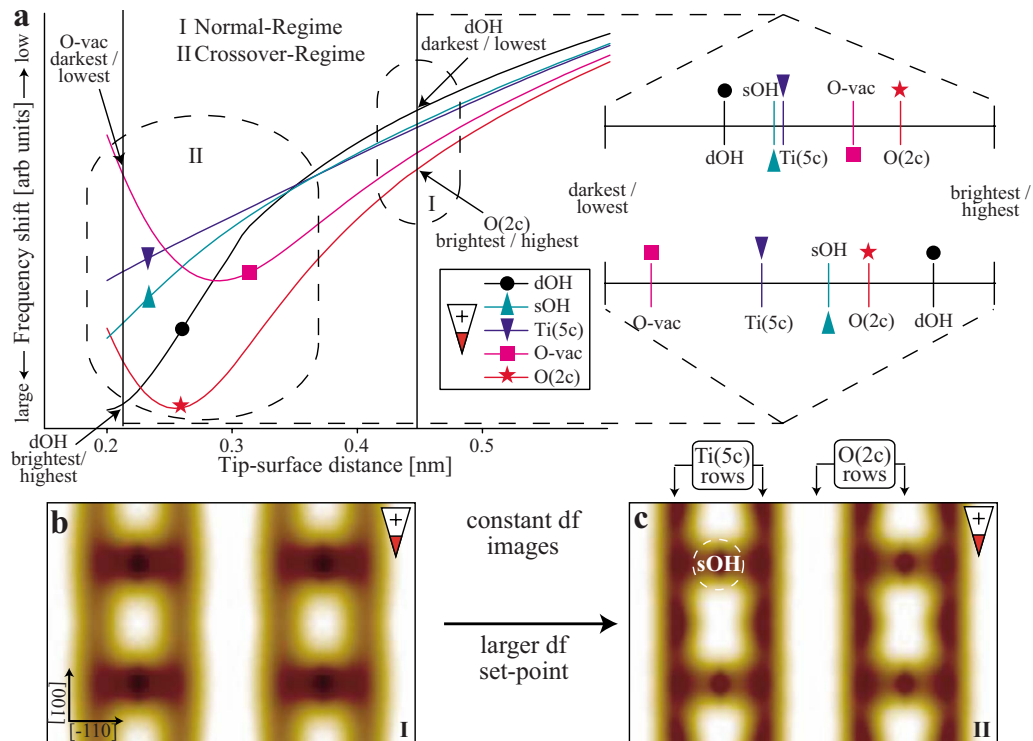
FIG. 6. (Color online) (a) Graph with five df vs distance curves used for identifying the imaging contrast of the different species on the surface as a function of tip-surface separation distance. The zero-point for the x axis is the relaxed position of the $O(2c)$ atoms. The vertical guidelines at $x \sim 0.21$ nm and $x \sim 0.45$ nm have been rotated and are depicted on the right, showing the relative cross points for the different curves. [(b) and (c)] Simulated constant frequency shift images of four sOH equidistantly placed along every second $O(2c)$ rows. (c) was simulated at a larger (more negative) frequency shift set point than (b). Image size=2.6×1.8 nm^2.

$3(a)$, and the imaging regime where this ordering is valid is labeled the normal regime. The simulated constant frequency shift image in the normal regime shows bright $O(2c)$ rows relative to the dark $Ti(5c)$ rows with the sOH imaged as well-defined dark holes with the same contrast as the $Ti(5c)$ rows, confirming the agreement between the theoretically df vs distance curves and experimental images. At a closer tip-surface distance corresponding to the vertical guideline at 0.21 nm in Fig. $6(a)$, the situation is markedly different. Now, the dOH groups are imaged as the highest, followed by $O(2c)$, sOH, $Ti(5c)$, and O-vac in order of decreasing height. The predicted height of the sOH as being in between that of the $Ti(5c)$ and that of the $O(2c)$ rows matches nicely with the measured ΔC_{Ti-O} and ΔH_{Ti-sOH} for the small tip-surface distance as indicated in Fig. $3(d)$, and this imaging regime is labeled the crossover regime. In Fig. $6(c)$, the simulated image in the crossover regime is shown, and the signature of the sOH has weakened noticeably. The contrast of the sOH is now slightly brighter compared with the dark $Ti(5c)$ rows, and the width along the [001] direction has been reduced, which is again in qualitative agreement with the experimental findings. At very small tip-surface imaging distances, the positively terminated tip causes significant displacement of the hydrogen proton in the OH group away from the tip, reducing the screening of the underlying bridging oxygen atoms, and the overall interaction is a convolution between the electrostatically positive tip apex, positive hydrogen, and the exposed negative oxygen ion. For certain tips and tip-

surface distances, we expect this convolution to result in the interaction over $O(2c)$ and over sOH being similar, and the signature of the sOH may vanish—explaining the apparent "stoichiometric" images seen in the experiment.

It is furthermore noted from the df vs distance curves in Fig. $6(a)$ that since the $Ti(5c)$ and the $O(2c)$ curves run almost parallel, the ΔC_{Ti-O} should remain almost constant independent of the tip-surface distances, which is in agreement with the experimentally measured values for ΔC_{Ti-O} as obtained from the images in Figs. $3(a)$ and $3(b)$. Also, the apparent increase in width of the dark $Ti(5c)$ rows with decreasing imaging distance, as evident from the experimental images in Figs. $3(a)$ and $3(b)$, is in good accordance with the simulated images in Figs. $6(b)$ and $6(c)$.

E. Covalent tip (neutral mode)

We have also imaged the surface in a third but rather rare mode shown in Fig. $7(a)$, which does not fit into the models discussed above, explaining the contrast by an electrostatically charged (positive or negative) atom terminating the AFM tip. Instead, the surface appears in the nc-AFM images as one would expect from the geometry of the hydroxylated $TiO_2(110)$ surface [see Figs. $1(b)$–$1(d)$]. The $O(2c)$ rows are imaged bright relative to the dark $Ti(5c)$ rows, with even brighter protrusions lying directly on top of the bright $O(2c)$ rows, reflecting the position of the hydrogen atoms belonging to the sOH groups. The ΔC_{Ti-O} and the height of the sOH
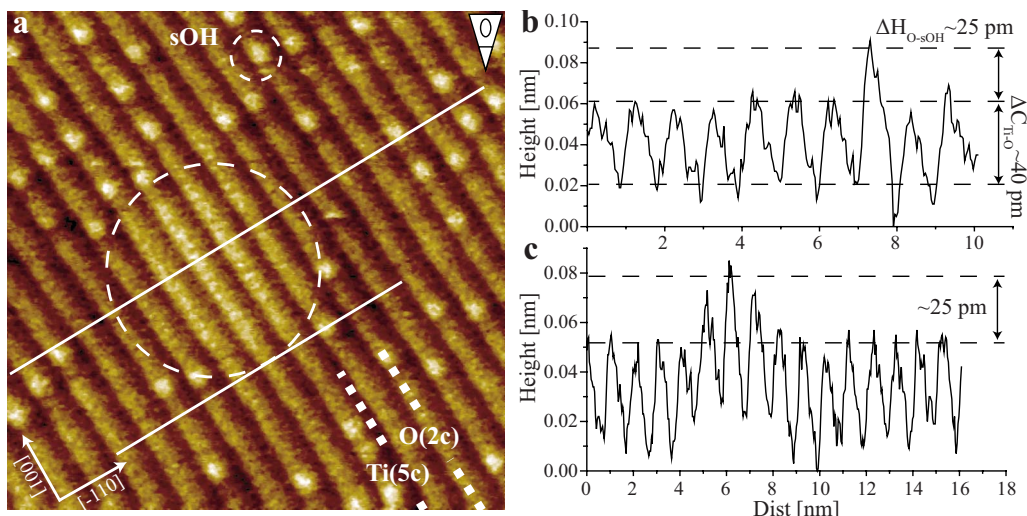
FIG. 7. (Color online) (a) Constant frequency shift nc-AFM image of the TiO$_2$(110) surface, recorded ~6 h and 34 min after preparation. The bright parallel lines are the O(2c) rows and the bright protrusions on top of the bright rows are sOH. [(b) and (c)] Cross sections taken along the two white solid lines in the [−110] direction in (a). The large white dotted circle indicates a charge patch imaged slightly higher than the unperturbed surface. IP: $df=−53$ Hz, Ampl$_{p-p}\approx 25$ nm, $U_{bias}=0.95$ V, and size=15×15 nm^2.

relative to the bright O(2c) rows are measured to be ~40 and ~25 pm, respectively. A similar image contrast was previously reported by Fukui *et al.* in Ref. 4. We explain this finding in terms of an electrostatically neutral and weakly interacting tip apex, and a possible tip termination could be that of a pure silicon tip. A silicon tip is generally considered to bind covalently to most surfaces, and such a silicon tip has theoretically been shown to produce bright contrast on the O(2c) rows relative to the dark Ti(5c) rows.[44] However, there have so far been no published results of the imaging of a sOH group with a silicon tip, and simulating a nc-AFM image of this mode is beyond the scope of this work. In first-principles simulations of the interaction of a silicon tip with the MgO surface,[45] we found the interaction with the adsorbed hydrogen to be stronger than with surface oxygen and the interaction with magnesium to be much weaker. This finding further supports the argument that a silicon tip is the source of the neutral-mode images.

The bright, rather large area in the center of the image in Fig. 7(a), indicated by the dashed circle, is likely to be of the same origin as similar features visible in STM experiments,[46] namely, charged subsurface impurities, which leads to changes in the local electronic structure. It is evident from STM images of the TiO$_2$(110) surface, both from our experience and that of others,[38,47] that hydroxyls (and O-vac) are repelled by these charge patches (or subsurface impurities) which also seems to be the case for the image presented in Fig. 7(a). It may seem unlikely that the image in Fig. 7(a) has been recorded with an electrostatically neutral tip, since it detects the charged subsurface impurities producing a large area of brighter contrast. The cross-section graph in Fig. 7(c) indicates that the bright area is imaged ~25 pm higher relative to the unperturbed surface. This observation can be explained by the fact that since the local electronic structure is altered by the subsurface impurities, so is the local surface potential or local work function. This alternation leads to an

uncompensated change in the contact potential difference between the surface and the tip, resulting in an additional attractive contribution to the force, a positive contribution to the force gradient, and ultimately an increased negative frequency shift, causing the area to be imaged slightly higher.[48,49]

F. Statistical analysis of different tip terminations and imaging modes

It is interesting to analyze the probability of a certain type of tip appearing, since the manufacturing of a nanotip suitable for atomic resolution, either by accidental or controlled contact of an AFM tip with the surface being imaged, must be considered as the outcome of a stochastic process. The possibilities are numerous when taking into account the detailed structure and composition of the resulting nanotip, but our experiments clearly show that atomic resolution on a TiO$_2$(110) surface comes only in the three generic categories analyzed above. Based on a very large statistical data set consisting of more than 500 atom-resolved images, we generally observed the electrostatic tip terminations (positive or negative) to be by far the most dominant, accounting for more than 95% of the total atomic-resolved images, split almost equally between the positively tip-terminated protrusion mode and the negatively tip-terminated hole mode. The remaining of less than 5% is identified as neutral-mode images most likely recorded with a pure silicon tip. This strong statistical bias toward the electrostatically terminated tips must reflect the statistical process of fabricating a sharp nanotip *in situ* by (gently) touching the surface with the tip. Intuitively, it makes sense that the tip is more likely to pick up or drop some TiO$_x$ material or rearrange polar material already present on the tip, compared with the event for the tip to drop all polar material including the native SiO$_x$ layer present on new tips, exposing a pure Si tip. Images recorded
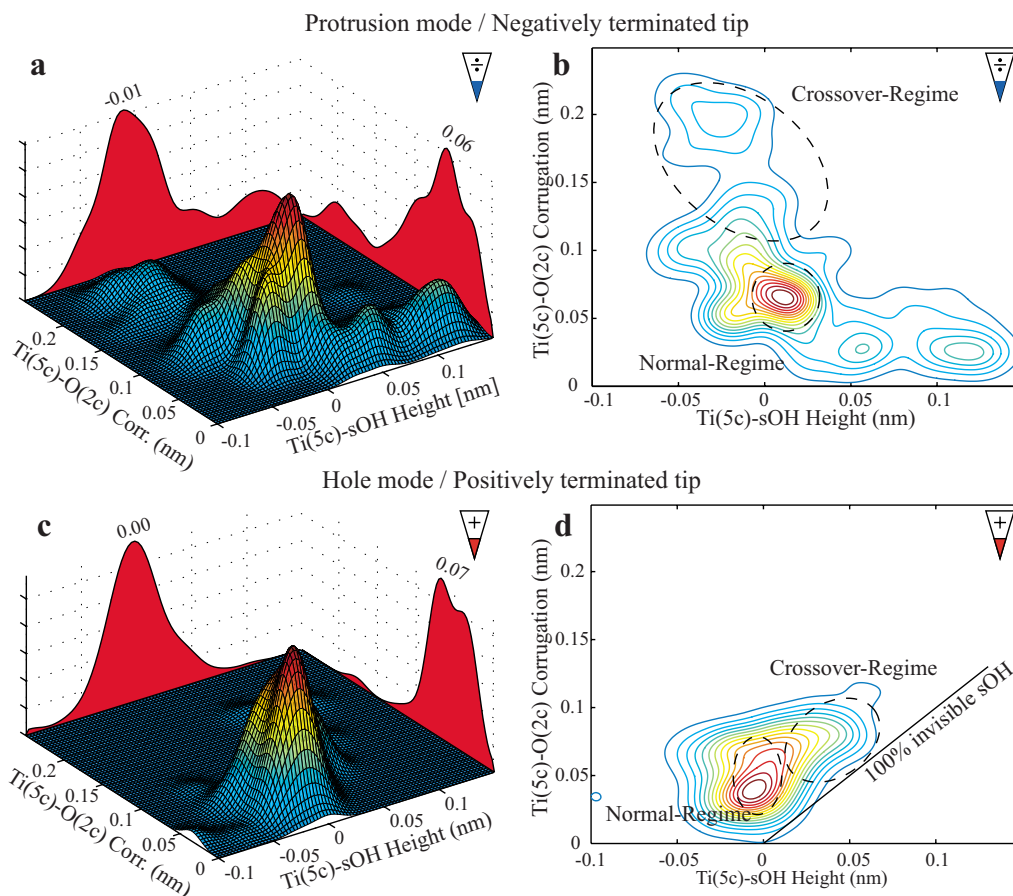
FIG. 8. (Color online) [(a) and (c)] Statistical analysis (3D Gaussian histograms) of corresponding Ti(5c)-O(2c) corrugations and Ti(5c)-sOH heights for the protrusion- and hole-mode images, respectively. On the sides of the 3D plot (xz plane for $y=0.25$ and yz plane for $x=0.15$), drawn are normalized curves representing integrals along constant x and y values, indicating the relative abundance of an independently measured parameter. (b) and (d) are contour plots of (a) and (c), respectively. Imaging regimes are indicated by dashed circles. In (d), a solid black line indicating where sOH would have exactly the same contrast as O(2c) making them invisible has been added.

with a hydrogen (Si-H) or hydroxyl (Si-OH) terminated tip were tested theoretically and gave almost no nc-AFM contrast, and this could then account for the experimental observations (not shown) where a small tip change resulted in a significant deterioration or complete loss of the atomic contrast.

To analyze the imaging parameter space associated with different levels of contrasts attainable within each of the two predominating imaging modes in more detail, we made a thorough statistical analysis of corresponding $\Delta C_{\text{Ti-O}}$ and $\Delta H_{\text{Ti-sOH}}$ values measured from a very large set of 373 experimental nc-AFM images. It is evident from the df vs distance curves in Figs. 5(a) and 6(a) that $\Delta C_{\text{Ti-O}}$ and $\Delta H_{\text{Ti-sOH}}$ are intimately linked throughout the imaging distance range, in a unique way depending on the contrast mode. The analysis presented here verifies that we are, in fact, able to probe the entire imaging distance range, revealing also the dominating level of image contrast of both linked $\Delta C_{\text{Ti-O}}$ and $\Delta H_{\text{Ti-sOH}}$, but also independently measured $\Delta C_{\text{Ti-O}}$ and $\Delta H_{\text{Ti-sOH}}$ values, within each of the imaging modes. Figures 8(a) and 8(c) are three-dimensional (3D) Gaussian histograms, where each point in the xy plane is given the following z value:

$$\sum_{i}^{all} \exp\left(- \frac{[x - \text{height}(i)]^2}{k_x^2} - \frac{[y - \text{corr}(i)]^2}{k_y^2} \right),$$

where "height" and "corr" are arrays containing the experimentally measured and corresponding $\Delta C_{\text{Ti-O}}$ and $\Delta H_{\text{Ti-sOH}}$ values, respectively. The decay constants k_x and k_y are taken to be the approximate uncertainties for the experimentally measured values, and in this case, both constants were set to 0.015 nm. This way of producing statistical histograms is superior to the more common bin-type histograms,[50] as the shape of these latter ones and, therefore, the conclusions drawn from them often depend critically on the chosen bin sizes and bin positions. For the histogram discussed here, there are no adjustable parameters, as the decay constant is intuitively set to the measurement uncertainty. In this way, each measurement point is given as a weighted distribution, rather than a delta-function-like peak. On the sides of the 3D plots in Figs. 8(a) and 8(c), two curves are depicted. They indicate the value of integrals along constant x and y values, and the curves are then subsequently scaled to match the maximum z value of the corresponding 3D plot for better presentation. As such, the curves represent the relative dis-

tribution of independently measured $\Delta C_{\text{Ti-O}}$ and $\Delta H_{\text{Ti-sOH}}$, respectively, and the most abundant value is indicated on the graphs. It is evident from these distribution curves that the attainable values for both $\Delta C_{\text{Ti-O}}$ and $\Delta H_{\text{Ti-sOH}}$ are spread out over a much wider range for the protrusion-mode images compared with the hole-mode images. The graphs in Figs. 8(b) and 8(d) are contour plots of the 3D Gaussian histograms in Figs. 8(a) and 8(c), respectively, and here again the difference in measurable values is evident. This apparent difference in attainable $\Delta C_{\text{Ti-O}}$ and $\Delta H_{\text{Ti-sOH}}$, between the protrusion-mode and the hole-mode images, is in perfect accordance with the *df* vs distance curves in the graphs in Figs. 4(a) and 6(a). For the protrusion-mode graph [negatively terminated tip, Fig. 4(a)], the curves for the O(2c) and Ti(5c) diverge from each other as the tip-surface distance is decreased, indicating that in a constant frequency shift measurement, the $\Delta C_{\text{Ti-O}}$ would increase with an increasing *df* set point. Also, the vertical distance between the Ti(5c) and sOH curves varies significantly over the tip-surface distance range. For the hole-mode graph [positively terminated tip, Fig. 6(a)], the situation is different. Here, the Ti(5c), O(2c), and sOH curves run much more parallel, indicating that the relative measurable height difference between these species will vary significantly less with the tip-surface imaging distance.

If we analyze the contour plot for the protrusion-mode measurements in Fig. 8(b) in more detail, we find that the connection between $\Delta C_{\text{Ti-O}}$ and $\Delta H_{\text{Ti-sOH}}$, as previously argued for, is very clear: an increase in $\Delta C_{\text{Ti-O}}$ is coupled to a decrease (or negative increase) in $\Delta H_{\text{Ti-sOH}}$. The large peak in the center of the contour plot, where $\Delta H_{\text{Ti-sOH}}$ is moderately positive and the $\Delta C_{\text{Ti-O}}$ is relatively low, corresponding to the normal regime in the graph in Fig. 5(a) and the image in Fig. 2(a), statistically dominates the graph and is as such the most probable way of imaging the TiO$_2$(110) surface. The peak in the top-left corner corresponds to the crossover regime in Fig. 5(a), where $\Delta C_{\text{Ti-O}}$ is huge and $\Delta H_{\text{Ti-sOH}}$ becomes more and more negative, matching the image in Fig. 2(b). The peak in the bottom-right corner of the contour plot in Fig. 8(b), where $\Delta H_{\text{Ti-sOH}}$ is relatively large and $\Delta C_{\text{Ti-O}}$ is very low and almost vanishing, does not seem to fit anywhere on the *df* vs distance graph in Fig. 5(a). We tentatively explain these experimental data as images taken with an atomically blunt tip containing a mixture of both anion and cation apex atoms, perhaps a TiO$_2$ nanocluster sitting in registry with the surface ions, so that the Ti(5c)-O(2c) geometric corrugation is almost exactly canceled out by the electrostatic interactions between the ions in the tip and surface.

It has previously been shown how the exact arrangement of the ions in the tip apex relative to the surface ions can have a large influence on the imaging contrast.[51,52] For the situation depicted here, it could destroy the atomic resolution on the ideal stoichiometric surface, leaving only the appearance of point defects, such as oxygen vacancies and hydroxyls that would break the tip-surface symmetry, to be visible. The contour plot for the hole-mode images in Fig. 8(d) is more difficult to divide into normal regime and crossover regime since $\Delta C_{\text{Ti-O}}$ and $\Delta H_{\text{Ti-sOH}}$ vary significantly less. A solid black line has been added in Fig. 8(d), labeled

"100% invisible sOH," indicating that for measurement points directly on top of this line, the sOH would be completely invisible and therefore immeasurable. The two regimes are indicated in the plot, with the normal regime assigned to the central and statistically dominating region with $\Delta H_{\text{Ti-sOH}} \sim 0$, and the crossover regime assigned to the region with comparable $\Delta H_{\text{Ti-sOH}}$ and $\Delta C_{\text{Ti-O}}$, close to the 100% invisible sOH line.

G. Splitting of dOH and dynamics of sOH groups revisited by noncontact atomic force microscopy

The dynamic splitting of dOH originally formed by the dissociation of water molecules at O-vac sites into two sOH located on separate O(2c) rows has been extensively studied by STM,[25] but the process has not earlier been investigated
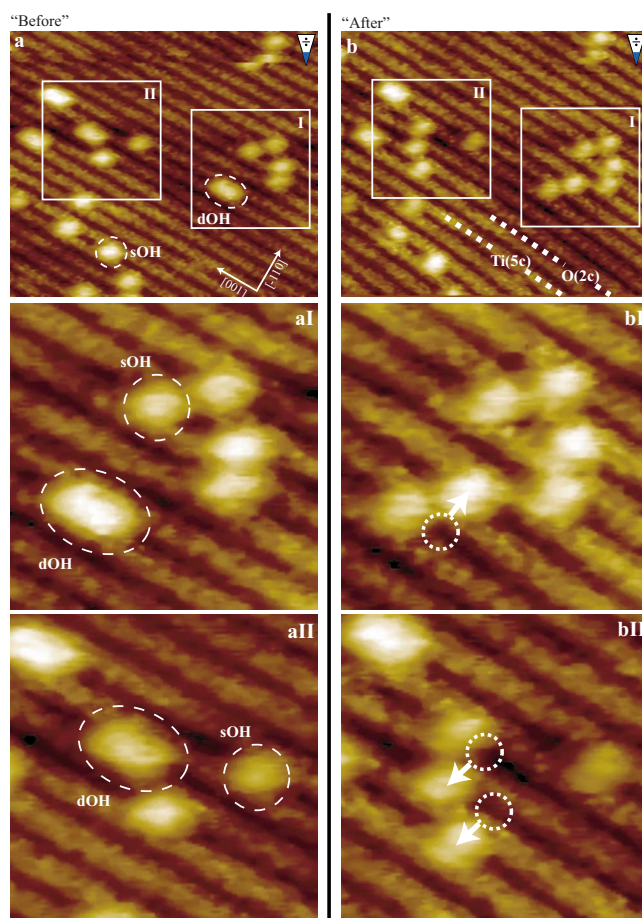

FIG. 9. (Color online) [(a) and (b)] Constant frequency shift nc-AFM images of the TiO$_2$(110) surface, recorded directly after each other at 1 h and 5 min and 1 h and 12 min after preparation, respectively. The bright lines along the [001] direction are the Ti(5c) rows and the bright protrusions lying in between these bright rows are identified as sOH and dOH. Two white squares (labeled "I" and "II") are indicated in (a) and (b), shown as zoom ins (aI)–(bII). The white dotted circles and arrows indicate where the sOH resided in the previous image and where it has moved to. IPs for (a) (for (b)) are $df = -45$ Hz $(-55$ Hz), Ampl$_{\text{p-p}} \approx 25$ nm (25 nm), $U_{\text{bias}} = 0.93$ V (0.93 V), and size $= 10 \times 10$ nm^2 (10×10 nm^2).

by nc-AFM. The images presented in Figs. 9(a) and 9(b) have been recorded right after each other with a time lapse of 7 min. We assign the bright parallel rows as being the Ti(5c) rows and the bright features lying in between these bright rows as sOH and dOH, as indicated in the image. Two sets of identical squares have been outlined in both images, labeled (I) and (II), and zoom ins of these are shown in Figs. 9(aI), 9(aII), 9(bI), and 9(bII). A detailed comparison of the images in Figs. 9(aI) and 9(bI) and in Figs. 9(aII) and 9(bII) reveals a dynamic situation where the dOH split up into two sOH. The zoom ins in Figs. 9(aI) and 9(bI) show how the dOH in the lower left corner of the image in Fig. 9(aI) is split along the [−110] direction, forming two sOH placed on neighboring O(2c) rows, spaced one lattice site apart along the [001] direction. The dotted circle and arrow in Fig. 9(bI) indicate where the hydroxyl group resided in the previous picture (as part of a dOH) and in which direction it has moved forming and leaving behind a sOH. In Figs. 9(aII) and 9(bII), the dynamic splitting of the dOH in the center of Fig. 9(aII) is again evident. However, now also an isolated sOH has moved along the [1−10] direction. The mechanism that splits the dOH involves an interaction with molecular water adsorbed on the surface diffusing along the Ti(5c) rows. These water molecules are, however, not visible at room temperature using nc-AFM (nor STM) as they diffuse much too fast, with a diffusion barrier of only ∼0.5 eV.[53] The splitting of dOH and the diffusing of sOH have been well studied by STM,[25,38,54] and this process has been revealed by nc-AFM experiments here.

IV. CONCLUSIONS

We have presented a detailed and comprehensive analysis of nc-AFM images of rutile $TiO_2(110)$ surface and have, in particular, accounted for the dependency of tip-termination and tip-surface distances. We have investigated three possible and distinctly different contrast modes observed experimentally, referred to as protrusion mode, hole mode, and neutral mode. The protrusion and hole modes are very interesting since the imaging contrast is determined primarily by the chemical identity or, more precisely, the electrostatic polarity of the ions on the metal-oxide surface, and not by the vertical geometric positions as is commonly assumed. The contrast of the individual species and ions on the $TiO_2(110)$ surface is found to be close to the exact inverse for the protrusion and hole modes, and we have previously shown that the origin of this contrast inversion is related to the electrostatic polarity of the outermost tip-apex atom.[11] Here, we extend this analysis by also considering the dependency on the tip-surface distance during measurement and find that the appearance of the surface structures may exhibit significant variations for each of the contrast modes. Generally, we observed that the signatures associated with defects in each mode become weaker at small tip-surface distances, and in some cases, the signatures even seem to disappear giving the impression of a defect-free surface. Furthermore, we have presented a third and much less frequently observed type of nc-AFM imaging contrast on the $TiO_2(110)$ surface, namely, the neutral mode. In contrast to the two previous contrast modes, the neutral mode represents the geometric structure to a much larger degree, and the ionic polarity of the surface atoms seems to play a much less significant role for the contrast formation in this mode. We propose that a clean reactive silicon tip, with Si atoms terminating the tip, would image the surface in such a way. We have additionally shown how nc-AFM can be used to detect subsurface single impurity atoms in a metal oxide, which, using Kelvin probe force microscopy, could reveal the absolute change in local work function caused by such impurities. Finally, we have shown using nc-AFM the dynamic splitting of the dOH groups into two sOH separated by one surface unit cell in both the [−110] and the [001] direction, and also the diffusion of sOH along the [−110] direction is directly observed, which is all in agreement with previously published STM results.[25]

We believe that the work presented here is generally applicable and is not just confined to the $TiO_2(110)$ surface. As such, it may aid in the understanding of contrast modes, level of contrast, and contrast mechanisms on the wide range of ionic metal-oxide surfaces and insulators in general and help develop the nc-AFM as an analytic surface science tool capable of providing direct chemical identification of the species and atoms imaged.

ACKNOWLEDGMENTS

[1] G. Binnig, C. F. Quate, and C. Gerber, Phys. Rev. Lett. **56**, 930 (1986).

[2] F. J. Giessibl, Rev. Mod. Phys. **75**, 949 (2003).

[3] R. Garcia and R. Perez, Surf. Sci. Rep. **47**, 197 (2002).

[4] S. Morita, R. Wiesendanger, and E. Meyer, *Noncontact atomic force microscopy* (Springer, New York, 2002).

[5] G. Binnig and H. Rohrer, Surf. Sci. **126**, 236 (1983).

[6] F. J. Giessibl, Science **267**, 68 (1995).

[7] A. S. Foster and W. A. Hofer, *Scanning Probe Microscopes: Atomic Scale Engineering by Forces and Currents* (Springer, New York, 2006).

[8] W. A. Hofer, A. S. Foster, and A. L. Shluger, Rev. Mod. Phys. **75**, 1287 (2003).

[9] C. Barth, A. S. Foster, M. Reichling, and A. L. Shluger, J. Phys.: Condens. Matter **13**, 2061 (2001).

[10] A. S. Foster, C. Barth, A. L. Shluger, and M. Reichling, Phys.

Rev. Lett. **86**, 2373 (2001).

[11] J. V. Lauritsen, A. S. Foster, G. H. Olesen, M. C. Christensen, A. Kühnle, S. Helveg, J. R. Rostrup-Nielsen, B. S. Clausen, M. Reichling, and F. Besenbacher, Nanotechnology **17**, 3436 (2006).

[12] R. Perez, M. C. Payne, I. Stich, and K. Terakura, Phys. Rev. Lett. **78**, 678 (1997).

[13] S. H. Ke, T. Uda, I. Stich, and K. Terakura, Phys. Rev. B **63**, 245323 (2001).

[14] A. S. Foster, A. Y. Gal, J. D. Gale, Y. J. Lee, R. M. Nieminen, and A. L. Shluger, Phys. Rev. Lett. **92**, 036101 (2004).

[15] R. Hoffmann, C. Barth, A. S. Foster, A. L. Shluger, H. J. Hug, H. J. Guntherodt, R. M. Nieminen, and M. Reichling, J. Am. Chem. Soc. **127**, 17863 (2005).

[16] C. L. Pang, O. Bikondoa, D. S. Humphrey, A. C. Papageorgiou, G. Cabailh, R. Ithnin, Q. Chen, C. A. Muryn, H. Onishi, and G. Thornton, Nanotechnology **17**, 5397 (2006).

[17] D. Matthey, J. G. Wang, S. Wendt, J. Matthiesen, R. Schaub, E. Lægsgaard, B. Hammer, and F. Besenbacher, Science **315**, 1692 (2007).

[18] R. Bennewitz, A. S. Foster, L. N. Kantorovich, M. Bammerlin, C. Loppacher, S. Schar, M. Guggisberg, E. Meyer, and A. L. Shluger, Phys. Rev. B **62**, 2074 (2000).

[19] R. Hoffmann, L. N. Kantorovich, A. Baratoff, H. J. Hug, and H. J. Guntherodt, Phys. Rev. Lett. **92**, 146103 (2004).

[20] M. Heyde, M. Sterrer, H. P. Rust, and H. J. Freund, Appl. Phys. Lett. **87**, 083104 (2005).

[21] C. Barth and C. R. Henry, Phys. Rev. Lett. **91**, 196102 (2003).

[22] Y. Namai, K. I. Fukui, and Y. Iwasawa, Catal. Today **85**, 79 (2003).

[23] S. Gritschneder and M. Reichling, Nanotechnology **18**, 044024 (2007).

[24] C. Barth and M. Reichling, Nature (London) **414**, 54 (2001).

[25] S. Wendt, J. Matthiesen, R. Schaub, E. K. Vestergaard, E. Lægsgaard, F. Besenbacher, and B. Hammer, Phys. Rev. Lett. **96**, 066107 (2006).

[26] T. R. Albrecht, P. Grutter, D. Horne, and D. Rugar, J. Appl. Phys. **69**, 668 (1991).

[27] M. Nonnenmacher, M. P. O'Boyle, and H. K. Wickramasinghe, Appl. Phys. Lett. **58**, 2921 (1991).

[28] U. Zerweck, C. Loppacher, T. Otto, S. Grafström, and L. M. Eng, Phys. Rev. B **71**, 125424 (2005).

[29] D. H. Gay and A. L. Rohl, J. Chem. Soc., Faraday Trans. **91**, 925 (1995).

[30] P. V. Sushko, A. S. Foster, L. N. Kantorovich, and A. L. Shluger, Appl. Surf. Sci. **145**, 608 (1999).

[31] A. V. Bandura and J. D. Kubicki, J. Phys. Chem. B **107**, 11072 (2003).

[32] R. W. Grimes, C. R. A. Catlow, and A. M. Stoneham, J. Phys.: Condens. Matter **1**, 7367 (1989).

[33] A. I. Livshits, A. L. Shluger, A. L. Rohl, and A. S. Foster, Phys. Rev. B **59**, 2436 (1999).

[34] L. Bergström, Adv. Colloid Interface Sci. **70**, 125 (1997).

[35] U. Diebold, Surf. Sci. Rep. **48**, 53 (2003).

[36] S. Wendt *et al.*, Surf. Sci. **598**, 226 (2005).

[37] R. Schaub, P. Thostrup, N. Lopez, E. Lægsgaard, I. Stensgaard, J. K. Nørskov, and F. Besenbacher, Phys. Rev. Lett. **87**, 266104 (2001).

[38] Z. Zhang, O. Bondarchuk, B. D. Kay, J. M. White, and Z. Dohnalek, J. Phys. Chem. B **110**, 21840 (2006).

[39] K. I. Fukui, H. Onishi, and Y. Iwasawa, Phys. Rev. Lett. **79**, 4202 (1997).

[40] The dOH curve has been calculated over the position exactly in between the two hydroxyl groups as this is the position of strongest interaction.

[41] A. S. Foster, C. Barth, A. L. Shluger, R. M. Nieminen, and M. Reichling, Phys. Rev. B **66**, 235417 (2002).

[42] M. A. Lantz, R. Hoffmann, A. S. Foster, A. Baratoff, H. J. Hug, H. R. Hidber, and H. J. Guntherodt, Phys. Rev. B **74**, 245426 (2006).

[43] S. Suzuki, K. I. Fukui, H. Onishi, and Y. Iwasawa, Phys. Rev. Lett. **84**, 2156 (2000).

[44] A. S. Foster, O. H. Pakarinen, J. M. Airaksinen, J. D. Gale, and R. M. Nieminen, Phys. Rev. B **68**, 195410 (2003).

[45] A. S. Foster and O. H. Pakarinen (unpublished).

[46] M. Batzill, K. Katsiev, D. J. Gaspar, and U. Diebold, Phys. Rev. B **66**, 235401 (2002).

[47] R. Schaub (private communication).

[48] J. M. R. Weaver and D. W. Abraham, J. Vac. Sci. Technol. B **9**, 1559 (1991).

[49] C. Loppacher, U. Zerweck, S. Teich, E. Beyreuther, T. Otto, S. Grafström, and L. M. Eng, Nanotechnology **16**, S1 (2005).

[50] L. Devroye and G. Lugosi, *Combinatorial Methods in Density Estimation* (Springer, New York, 2001).

[51] R. Oja and A. S. Foster, Nanotechnology **16**, S7 (2005).

[52] M. L. Sushko, A. Y. Gal, M. Watkins, and A. L. Shluger, Nanotechnology **17**, 2062 (2006).

[53] J. Matthiesen (private communication).

[54] O. Bikondoa, C. L. Pang, R. Ithnin, C. A. Muryn, H. Onishi, and G. Thornton, Nat. Mater. **5**, 189 (2006).

[55] S. J. Thompson and S. P. Lewis, Phys. Rev. B **73**, 073403 (2006).

[56] OH bond length is taken from our own calculations.